Available online at www.sciencedirect.com
ScienceDirect
Trans. Nonferrous Met. Soc. China 34(2024) 65−79
Transactions of Nonferrous Metals Society of China
www.tnmsc.cn

Mechanical properties and microstructural evolution of 5052 aluminum alloys by multi-pass stretching and induced electro-pulsing treatment

Shi-peng WANG[1], Xiao-hui CUI[1,2,3], Ang XIAO[2], Zhuo-xing YU[2], Zhi-hao DU[2]

1. Light Alloy Research Institute, Central South University, Changsha 410083, China;
2. College of Mechanical and Electrical Engineering, Central South University, Changsha 410083, China;
3. State Key Laboratory of High Performance Complex Manufacturing, Central South University, Changsha 410083, China

Received 22 June 2022; accepted 14 March 2023

Abstract: A compound-forming method that combines multi-pass stretching and induced electro-pulsing treatment (IEPT) is proposed. The effects of induced current on the microstructure and mechanical properties of material were investigated using transmission electron microscopy and electron backscatter diffraction measurements. The samples stretched by 5% each time showed 145% increase in elongation after 4 stretching and IEPT cycles. The IEPT caused "stress drop" in pre-deformed sheets, while the plasticity increased. Meanwhile, the dislocation density decreased, the deformation structure changed to the substructure, and the grain size increased slightly. The material anisotropy was reduced and a new ⟨111⟩//TD texture appeared after IEPT. The combination of electrical effect and Joule heating enhanced dislocation mobility and vacancy movement. The temperature distribution, with a maximum temperature reaching 144.7 °C, was simulated using ANSYS software. The theoretical calculation results were consistent with experimental data.

Key words: 5052 aluminium alloy; induced electro-pulsing; texture evolution; Joule thermal simulation; strength calculation

1 Introduction

Aluminum alloys are widely used in automotive and aerospace industries owing to their high specific strength and good corrosion resistance [1]. Material plasticity significantly reduces during the formation process due to accumulated strain and work hardening. Heat treatment processes like annealing are commonly utilized to improve material plasticity after deformation. However, the annealing process often takes longer times. For instance, 5052 aluminum alloys require more than 2 h of annealing, leading to a significant energy loss [2,3].

Electrically assisted forming processes could significantly increase the material plasticity while reducing the forming forces [4]. This can be achieved by applying an electric current to materials. The phenomenon associated with the decrease in rheological stress and increase in plastic deformability is referred to as the "electro-plastic effect" [5]. Numerous theories, including electron wind theory, thermal expansion, and Joule heating have been developed to explain the mechanism of the electroplasticity effect [6]. For instance, ZHANG et al [7] studied the evolution of dislocations in the presence of current by comparing electrical in-situ TEM with heated in-situ TEM experiments. YAN et al [8] noticed the fast dissolution of pure aluminum sub-boundaries into dense arrays of dislocations under applied

Corresponding author: Xiao-hui CUI, Tel: +86-15388028791, E-mail: cuixh622@csu.edu.cn
DOI: 10.1016/S1003-6326(23)66382-4

electric fields. LIU et al [9] studied the effect of pulsed current (PC) on AZ31B magnesium sheets and showed that dislocation annihilation is enhanced with the increase of peak current density and the decrease of pulsed frequency. ZHOU et al [10] carried out electropulsing-assisted creep aging (ECA) and conventional creep aging (CCA) tests at various stress levels and time intervals. The use of electropulsing resulted in a significant change in creep behavior, with a 17% increase in elongation.

For 5052-H32 aluminum alloys, ROH et al [11] conducted tensile elastoplasticity studies under pulsed currents. Their results showed similar electroplastic behavior under the same electrical field density but at different electrical pulse parameters. CHEN et al [12] studied the influence of electric pulse treatment (EPT) on the mechanical properties of 7075 aluminum alloy and recorded a 6.7% increase in material elongation at a pulse frequency of 200 Hz. The applied pulsed current changed the amount and distribution of the second precipitates while creating a precipitation-free zone around the grain boundary. YANG et al [13] compared the effects of EPT and annealing on the tensile behavior of steels after interrupted stretching. Their data revealed that EPT could restore material tensile properties and repair the void in the matrix when compared to annealing. GU et al [14] applied a high-density pulsed current to deformed nickel-based alloys and observed completely lifted strain hardening, restoring ductility to the alloy. DOBRAS et al [15] noticed an increase in the uniform strain of the supersaturated solid solution state of AA7075 aluminum alloy under a current density of 10 A/mm^2. The ductility of the material was enhanced by dislocation motion and annihilation due to the electron wind and Joule heating effect.

However, the current loading method and part shape are limitations of electro-assisted forming processes. Previous research suggested the induced electro-pulsing treatment (IEPT) based on electro-magnetic inductive law. The principle of this method is based on generating high-density induction pulse currents by varying pulsed magnetic fields, resulting in wider applications. XIAO et al [16] investigated the effects of induced pulse current on the mechanical properties and microstructure of 7075-T6 aluminum alloy after pre-stretching. Their results showed a slight decrease in strength coupled with a significant increase in elongation. However, this research only examined the effect of one-pass IEPT on material plasticity.

In this work, a composite forming method that combines multiple processes of stretching and IEPT is proposed. The stretching with fixed deformation amount led to work hardening. Afterward, the induced current was used to quickly eliminate the generated work hardening, further improving the formability of the material. Transmission electron microscopy (TEM), X-ray diffraction (XRD), and electron backscatter diffraction (EBSD) measurements were used to investigate the influence of pre-deformation and IEPT on the mechanical properties and microstructural evolution of the material. The induced current was found to cause current-induced annealing, reducing dislocation density, and transforming grain structure. Overall, the proposed composite forming method may improve the formability of work hardening alloys and provide a new electro-plastic process for rapid change of deformed material properties, which is suitable for future industrial needs.

2 Experimental

2.1 Materials and methods

Sheets of 5052-H32 aluminum alloy (1 mm thick) were used in this study. The chemical composition of the alloy is listed in Table 1, and the mechanical properties of 5052-H32 aluminum alloy (total elongation of 11%) are summarized in Table 2.

The experimental flow is displayed in Fig. 1. The experimental method consisted of first applying a fixed amount of stretch to the specimen.

Table 1 Chemical composition of 5052-H32 aluminum alloy (wt.%)

Si	Fe	Cu	Mn	Mg	Cr	Al
0.15	0.447	0.052	0.098	2.318	0.19	Bal.

Table 2 Mechanical properties of 5052-H32 aluminum alloy issued from tensile tests

Ultimate tensile stress/MPa	Yield stress/MPa	Total elongation/%
240	186	11

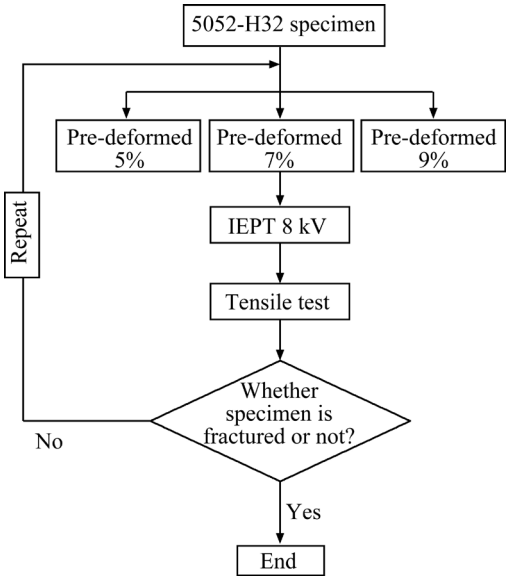

Fig. 1 Flowchart of experimental procedures

The pre-deformed material was then treated by an induced pulse current to increase the material elongation. Next, multiple passes of tensile and induced current treatments were utilized until the specimen started to fracture. Three sets of experiments were set up, consisting of 5%, 7%, and 9% stretch in each set. The discharge voltage was fixed to be 8 kV, and a unidirectional tensile test was carried out on a CMT−5504 electronic universal testing machine with a tensile speed of 2 mm/min.

2.2 Experimental set-up

The unidirectional tensile specimens with a gauge length of 67 mm and width of 12.5 mm are illustrated in Fig. 2(a), and the dimensions of coil construction are provided in Fig. 2(b). The coil shape consisted of runway type, and the cross-sectional area of the coil wire was set to be 3 mm × 10 mm. A schematic diagram of the experimentally induced current is shown in Fig. 2(c). It is worth noting that the bridge was in contact with the specimen to form an induced current circuit. The physical diagram of the experimental setup is provided in Fig. 2(d). A Lovelace coil and an oscilloscope were used to record the pulse current through the coil, providing data for Joule heating simulation.

2.3 Microstructural characterization

The microstructure of each material was observed by TEM (Talos F200X) and EBSD (Helios 5 CX−Edax). The sample area used for observation is shown in Fig. 2(a). The TEM samples were first thinned to 80−100 μm by water-grit sandpaper before being punched down to 3 mm (diameter) discs by a mechanical shear followed by electrolytic double-spray thinning in an electrolyte containing 30% nitric acid and 70% methanol at the voltage of 20 V. The samples used for EBSD experiments were prepared by standard metallo-

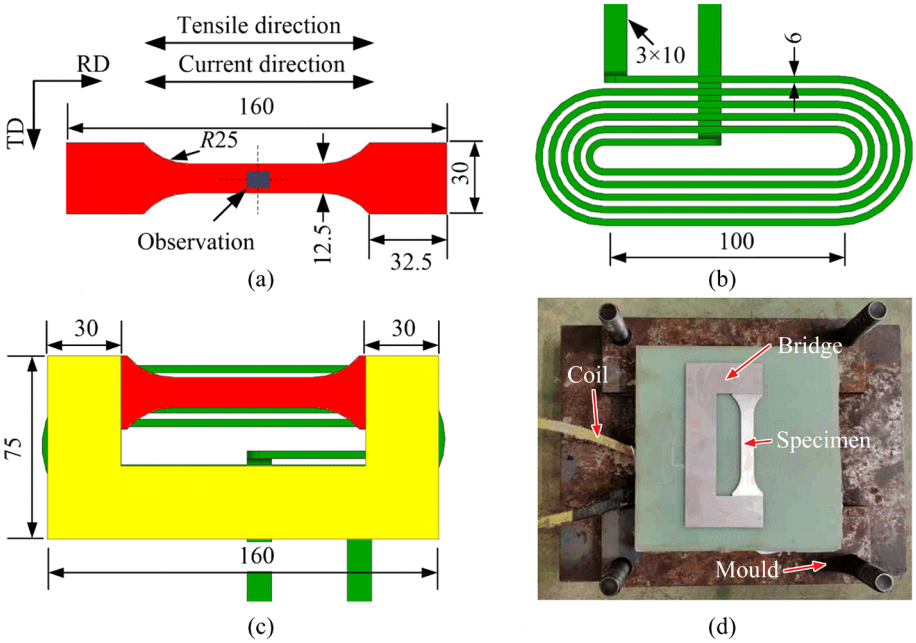

Fig. 2 Experimental set-up: (a) Dimensions of unidirectional tensile specimen; (b) Coils; (c) Schematic diagram of set-up; (d) Physical diagram of set-up (Unit: mm)

graphic grinding techniques. After grinding and polishing, electrolytic polishing was carried out in a solution composed of 10% perchloric acid and 90% ethanol at an experimental temperature of 20 °C and a voltage of 20 V for approximately 60 s. EBSD experiments were performed at the scan voltage of 20 kV and scan step of 0.9 μm. The dislocation density was measured by XRD (Rigaku D/max 2500PC) with Cu K_α radiation at 40 kV, 200 mA, scanning speed of 2 (°)/min, and scanning angle from 10° to 80°.

3 Results

3.1 Tensile performance

The engineering stress−strain curves of each experimental group are shown in Fig. 3. The stress decreased significantly after IEPT compared to the previous pre-deformation, resulting in a "stress drop" phenomenon. The final material elongation gradually increased for alternating pre-stretching and IEPT processes as the amount of fixed pre-deformation decreased and the number of IEPT treatments increased. The final material elongations reached 15.2%, 20.8%, and 27% under (9% stretching + discharge), (7% stretching + discharge), and (5% stretching + discharge), respectively. Compared to the original 5052-H32 material, the elongation increased by 38%, 89%, and 145%, respectively. Thus, the amount of fixed pre-stretching was closely related to the final material plasticity, where smaller pre-deformation achieved the largest elongations.

3.2 EBSD analysis

Specimens with 7% pre-deformation were selected to investigate the continuous change in microstructure using the EBSD technique. P_1, I_1, P_2, and I_2 in Fig. 3(c) were the microscopic observation sampling points. Point P_1 represented the specimen undergoing the first pre-deformation and I_1 denoted the specimen undergoing the first IEPT after pre-deformation. Points P_2 and I_2 represented the second pre-deformation and IEPT of the specimen, respectively. The EBSD grain maps at different observation points are provided in Figs. 4(a_1−d_1),

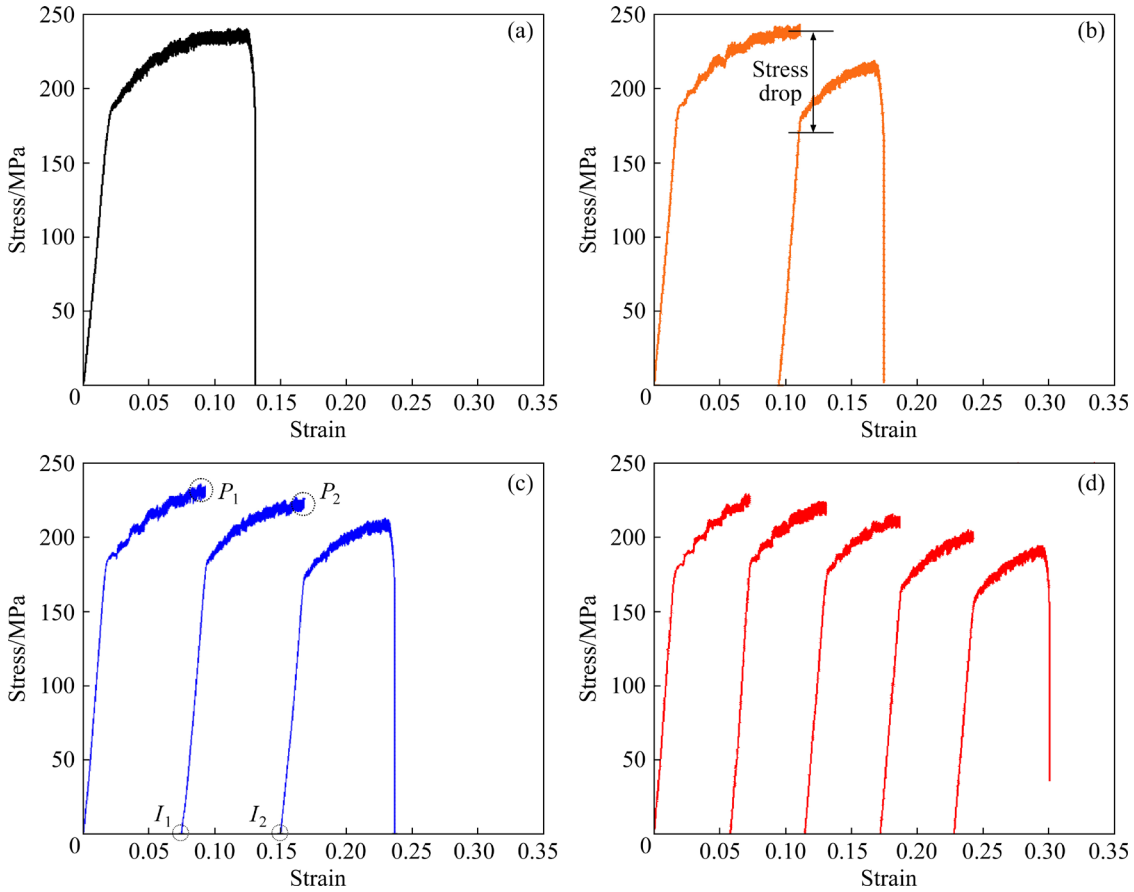

Fig. 3 Engineering stress−strain curves of original 5052-H32 sheet (a), (multiple stretching 9% + discharge 8 kV) (b), (multiple stretching 7% + discharge 8 kV) (c), and (multiple stretching 5% + discharge 8 kV) (d)

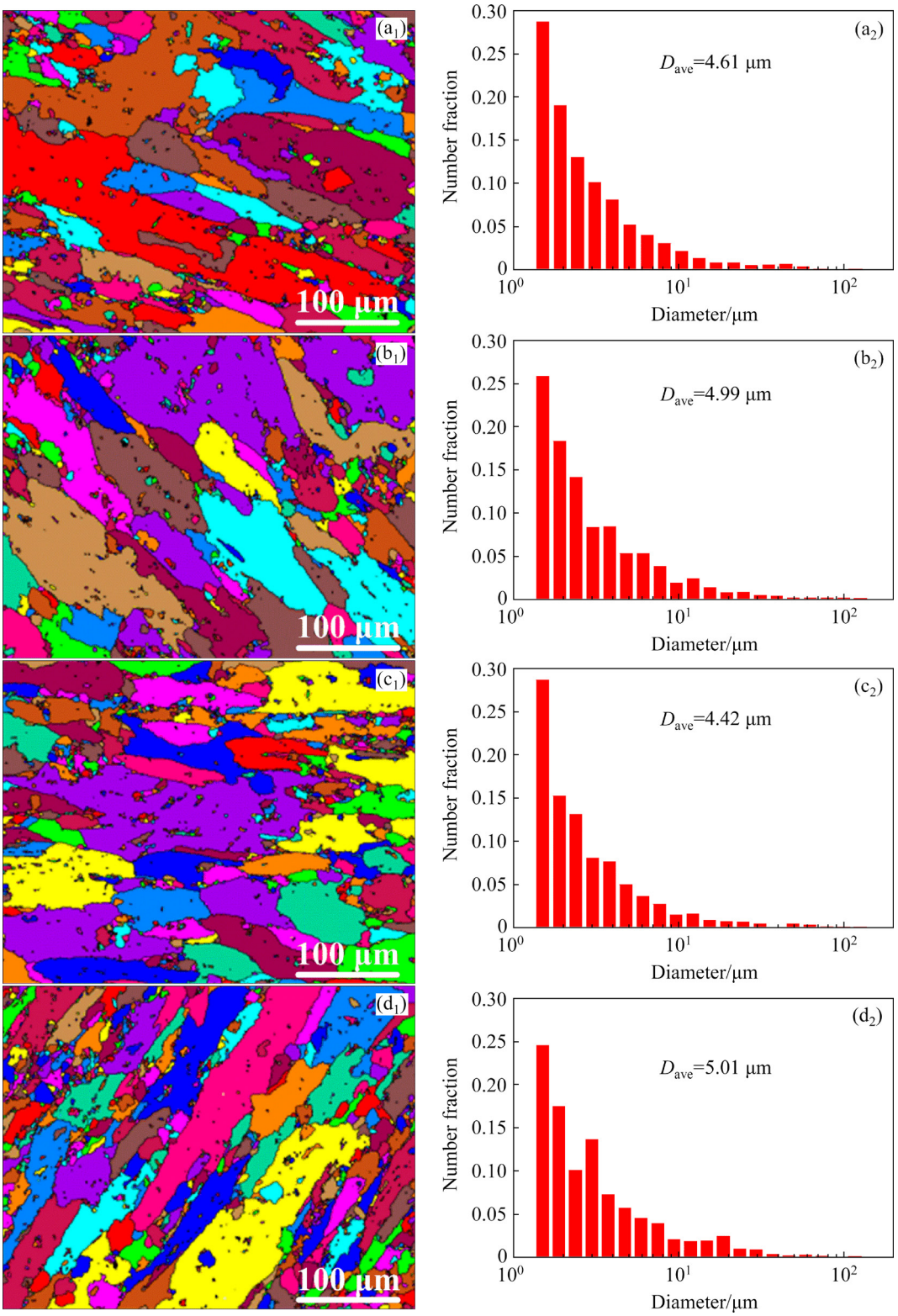

Fig. 4 EBSD grain maps (a_1−d_1) and grain size statistics (a_2−d_2) of points: (a_1, a_2) P_1; (b_1, b_2) I_1; (c_1, c_2) P_2; (d_1, d_2) I_2

and the corresponding grain size statistics are shown in Figs. 4(a_2−d_2). After the first pre-deformation, some grains were elongated, and many fine broken grains with a statistical average grain size of 4.61 μm were formed. The amount of small grains decreased after the first IEPT, while grain size increased slightly (4.99 μm). After the second pre-deformation, the specimen showed more small grains than the first IEPT due to re-work hardening that reduced the average grain size

(4.42 μm). The average grain size increased to 5.01 μm after the second IEPT, which may be related to the electrical effect of induced current and Joule heating, as previously reported [17].

Previous studies have suggested that EPT could increase the nucleation rate, reduce the temperature of dynamic recrystallization, and promote grain boundary sliding [18]. Oim-analysis software was used to investigate recrystallization behavior of materials. Figures 5(a−d) display the grain orientation spread (GOS) distribution of the specimens at Points P_1, I_1, P_2, and I_2, respectively. As shown, EBSD plots consisted of small numbers of recrystallized and sub-structured grains, as well as large numbers of deformed structures. A statistical plot of the corresponding GOS values is presented in Fig. 5(e). The grains were defined as recrystallized grains for GOS values below 1.5°, sub-structures for GOS values between 1.5° and 7°, and deformed structures for GOS values above 7°. The specimens showed large numbers of deformed grains at Points P_1 and P_2 due to pre-deformation. The proportion of deformed structures at Points I_1 and I_2 was reduced after IEPT. Compared to Point P_1, the percentage of deformed grains at Point I_1 declined from 66% to 56%. Compared to Point P_2, the percentage of deformed grains at Point I_2 reduced from 60% to 50%. The small content of recrystallized grains (<4%) indicated that deformed grains mainly transformed towards substructures. The

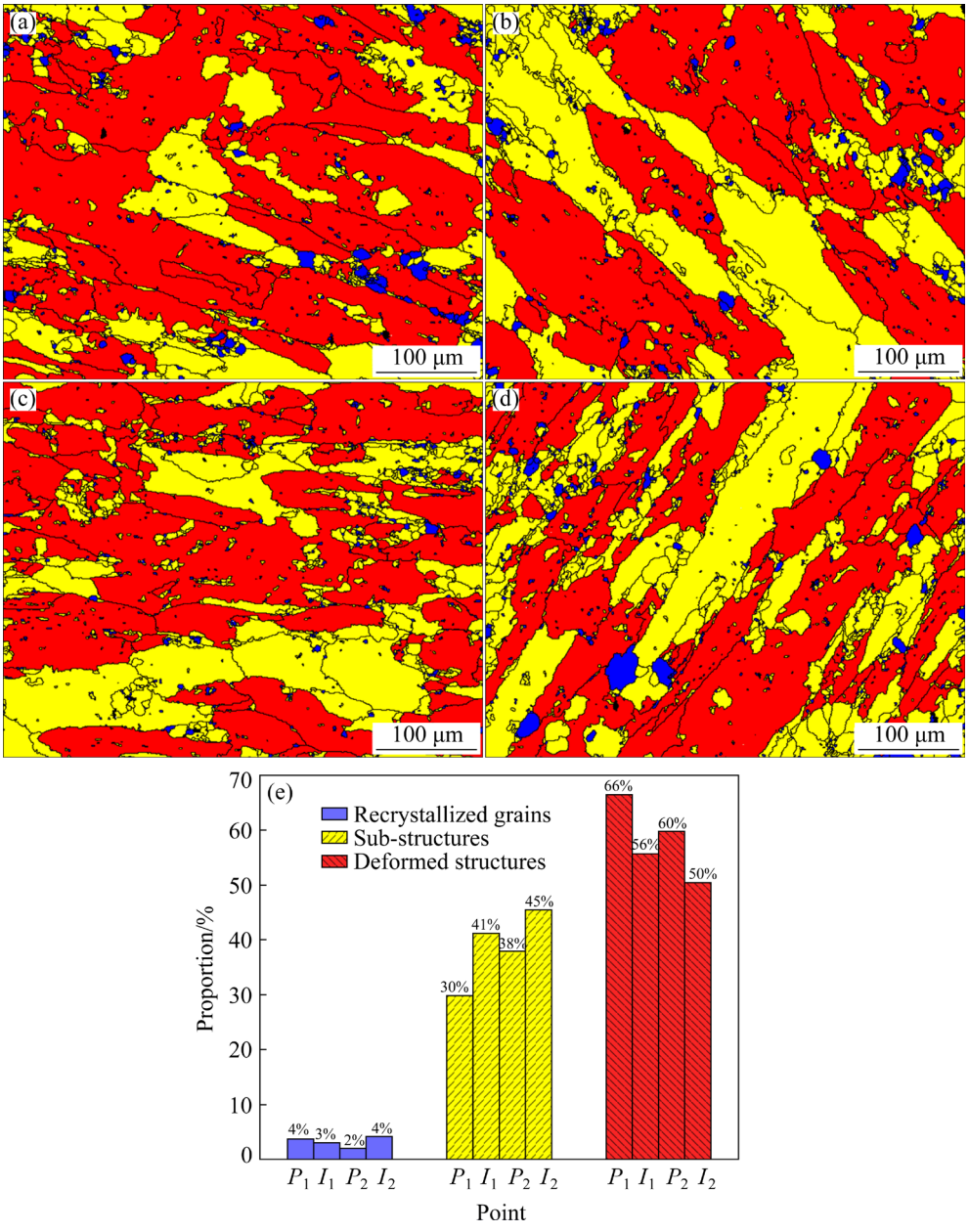

Fig. 5 GOS distribution diagrams of Points P_1 (a), I_1 (b), P_2 (c) and I_2 (d), and corresponding proportions (e)

work hardening and high-density dislocations of the material were produced by tensile pre-deformation. After IEPT, the application of induced current to specimens encouraged the rapid rearrangement of dislocations, leading to dynamic reversion and transformation of deformed structures into substructures [19]. Therefore, the application of IEPT to pre-deformed samples resulted in the transformation of deformed structures into substructures, mainly by the dynamic recovery effect. Also, high-density induced currents resulted in the formation of recovered substructures.

The evolutions of the inverse pole figure after pre-deformation and IEPT are displayed in Fig. 6. The inverse pole figure showed strong ⟨001⟩//RD and ⟨111⟩//RD textures at Point P_1, representing a stable orientation of FCC metal under uniaxial stretching [20], along with ⟨001⟩//TD textures. After the second pre-stretching treatment, the texture orientations in ⟨001⟩//RD and ⟨111⟩//RD were still clearly visible. The comparison of Figs. 6(b) and 6(d) showed that the texture changed after the induced current treatment. The ⟨111⟩//RD texture was deflected, while a new ⟨111⟩//TD texture appeared and the original ⟨001⟩//TD texture diminished. The induced current caused grain boundary migration and deflection of grain orientation, affecting the texture-concentrated orientation. Moreover, grain boundary movement is depended on the driving energy and Joule heating at grain boundaries [21]. IEPT reduced stress concentrations in the specimen and degraded the anisotropy of the material.

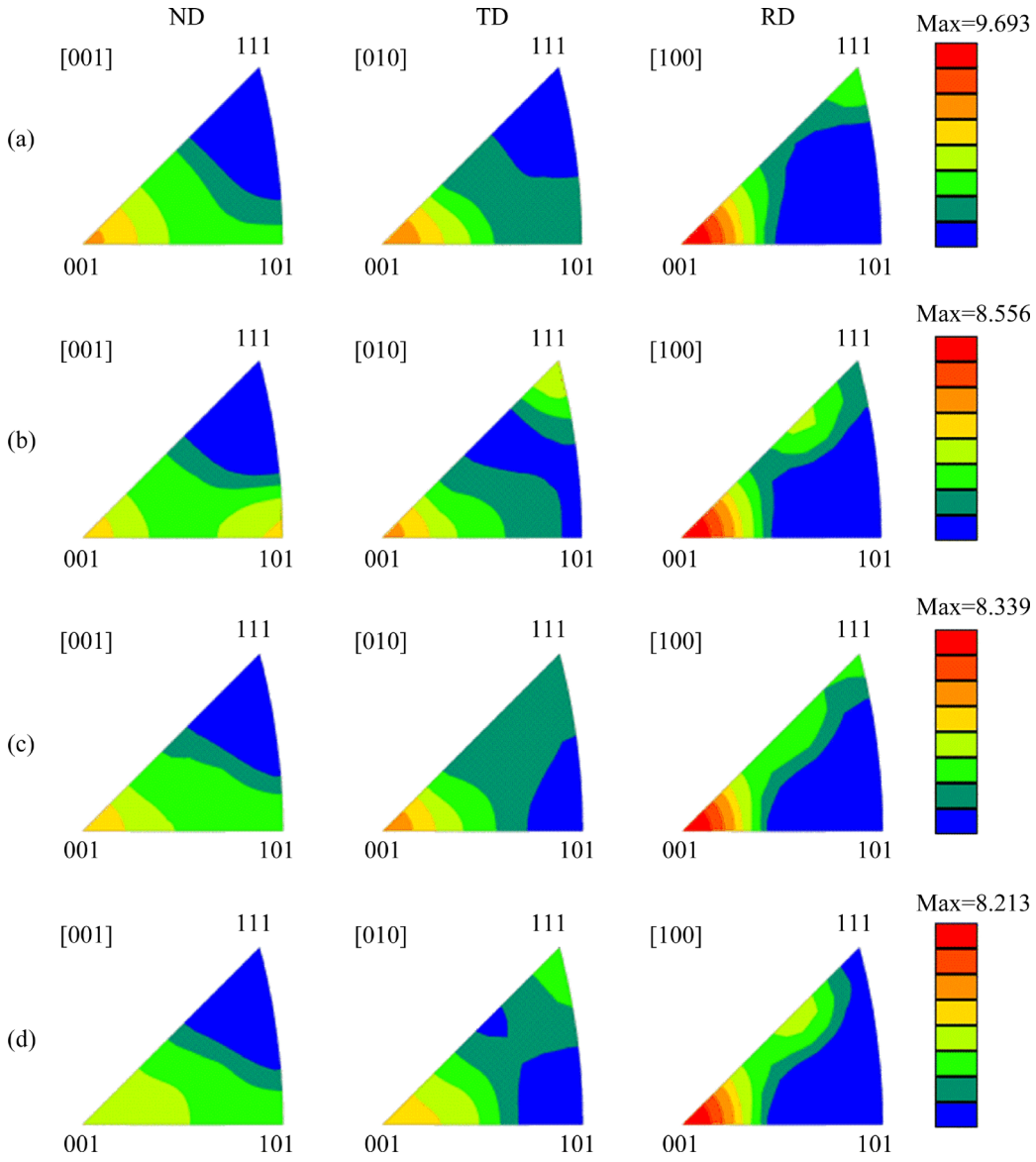

Fig. 6 Inverse pole figures of Points P_1 (a), I_1 (b), P_2 (c) and I_2 (d)

3.3 TEM characterization

To further study the impact of the induced current on the microstructure, the specimens were characterized by TEM imaging. Figure 7 shows TEM images of Points P_1 and I_1. Large numbers of dislocation tangles were observed (Figs. 7(a, c, e)), with dislocations interwoven in a web-like tangle after pre-stretching. As shown in Fig. 7(b), the dislocation density was significantly reduced, and dislocation entanglement decreased after IEPT. Figure 7(d) illustrates an individual grain observed at Point I_1 with dislocation moving toward the grain boundary within the grain, showing the characteristics of locally defect-free grains. After IEPT, the dislocation density was significantly reduced (Fig. 7(f)), with some dislocation annihilations and remaining dislocations showing uniform distributions. The change in dislocation morphology indicated that induced current increased dislocation mobility and annihilated accumulated dislocations at vacancies and structural distortion grain boundaries.

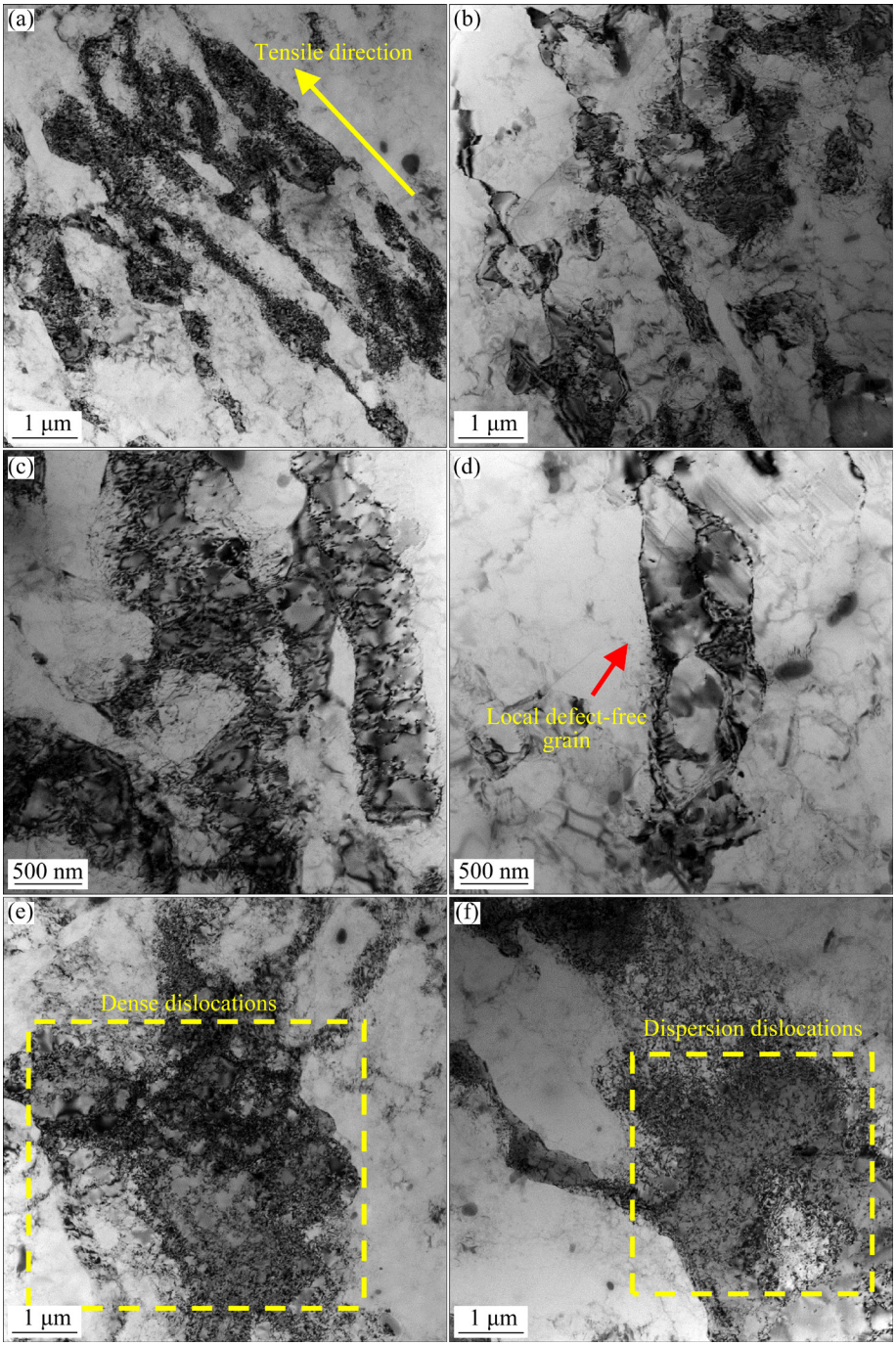

Fig. 7 TEM images of Points P_1 (a, c, e), and I_1 (b, d, f)

4 Discussion

4.1 Simulation of induced current and Joule heating

The effect of Joule heating caused by the current on the material should be considered when an induced pulse current passes through the metal. An oscilloscope was used to detect the loading current passing through the coil (Fig. 8(a)), and ANSYS/EMAG software was employed to simulate the distribution of induced current and temperature variation during testing. For electromagnetic field simulation, the element types used for the sample, bridge, coil, airfield, and far-field were all made of Solid 97. For temperature field simulation, Solid 70 was used as the element type. The sample thickness direction was divided into three layers of the grid. The bridge and coil were based on hexahedral grids with a size of 3 mm. The far-field boundary was defined as the point beyond which the electromagnetic field could no longer propagate. The material parameters used in simulation are listed in Table 3, and the induced current distribution at peak current is shown in Fig. 8(b). A current loop is formed between the specimen and the bridge, with a current density of 0.137×10^{11} A/m^2 at Node A.

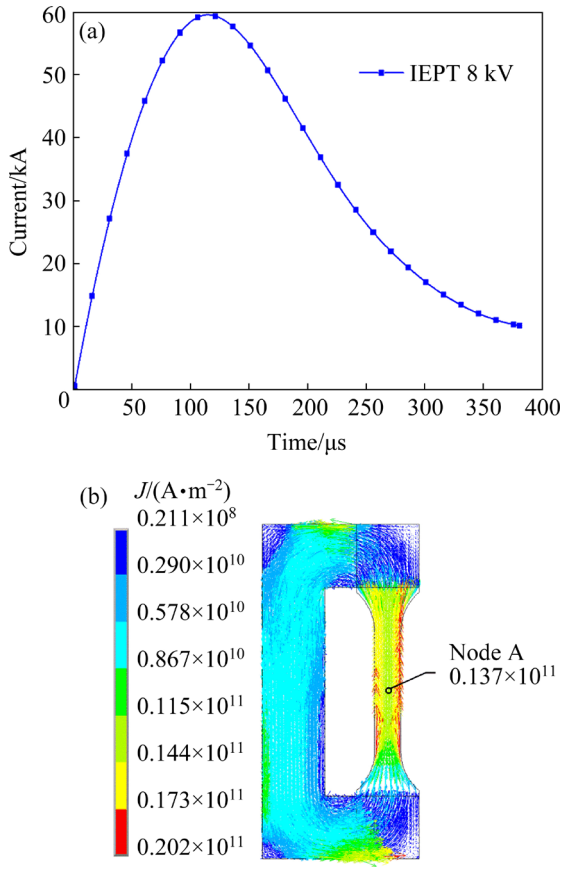

Fig. 8 Loaded current curve (a) and induced current density distribution (b)

Table 3 Simulation parameters of 5052-H32 aluminum alloy

Density/ (kg·m^{-3})	Resistivity/ (Ω·m)	Initial temperature/°C
2730	4.93×10^{-8}	20

By considering the effect of Joule heating, the thermal conductivity and specific heat capacity of the aluminum alloy changed with the rise in temperature during IEPT. The main material parameters obtained from China Aerospace Materials Manual are listed in Table 4. The above given current densities were set as an initial condition of the temperature field. The initial temperature of the sample was fixed at 20 °C. The temperature distribution of the specimen at the maximum temperature during IEPT is displayed in Fig. 9(a). The edge of the sample displayed a higher temperature due to the induced current caused by the coil structure. The temperature at Node A was extracted and plotted as a function of the time in Fig. 9(b). The maximum temperature at Node A was 144.7 °C, and specimen temperature during IEPT was much lower than the conventional annealing temperature for non-heat-treated aluminum alloys (335−405 °C). Moreover, the holding time at maximum temperature was quite short. The microstructural evolution and temperature results showed that large enhancements in elongation cannot be not only attributed to the temperature rise, but also due to the non-thermal effects under the action of the induced current.

Table 4 Material parameters of 5052 alloy used in this study

Temperature/ °C	Thermal conductivity/ (W·m^{-1}·°C^{-1})	Specific heat capacity/ (J·kg^{-1}·°C^{-1})
20	155	921
100	159	963
200	163	1005
300	163	1047

4.2 Changes in elongation

A significant increase in elongation occurred in the specimens after IEPT, which was closely related to the transformation of grain organization

and the change in dislocations. The introduction of pre-deformation and induced current changed the shape and orientation of grains. The Kernel average orientation (KAM) diagram was used to characterize the degree of uniformity of plastic deformation at the grain scale, with higher KAM values indicating higher degrees of plastic deformation or higher defect densities [22]. The KAM plots and statistical values of different groups of specimens are summarized in Fig. 10. The black lines in the graph represent high-angle grain boundaries with misorientation angles greater than 15°. After the first pre-deformation, Point P_1 underwent plastic deformation to yield high-density intra-grain dislocations with an average KAM of 1.786°. The intra-grain dislocation densities were reduced after IEPT, while small numbers of locally defect-free grains were observed. Consequently, the average KAM value was reduced to 1.678°. The same changes were noticed for Points P_2 and I_2, where the average KAM value first increased to 1.796° and then decreased to 1.650°. The reduction in KAM values after IEPT indicated a decline in the dislocation density of grains. In addition, the formed electron wind promoted the dislocation movement and untangling. Under the action of

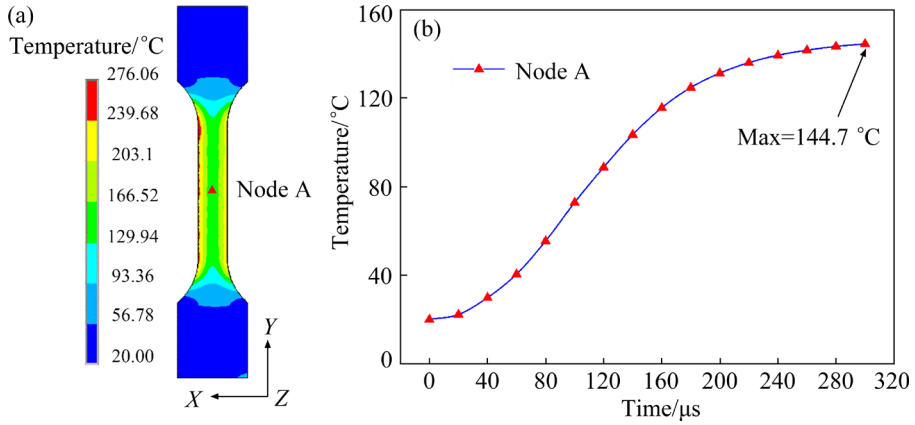

Fig. 9 Simulated temperature distribution (a) and temperature variation curve (b) at Node A

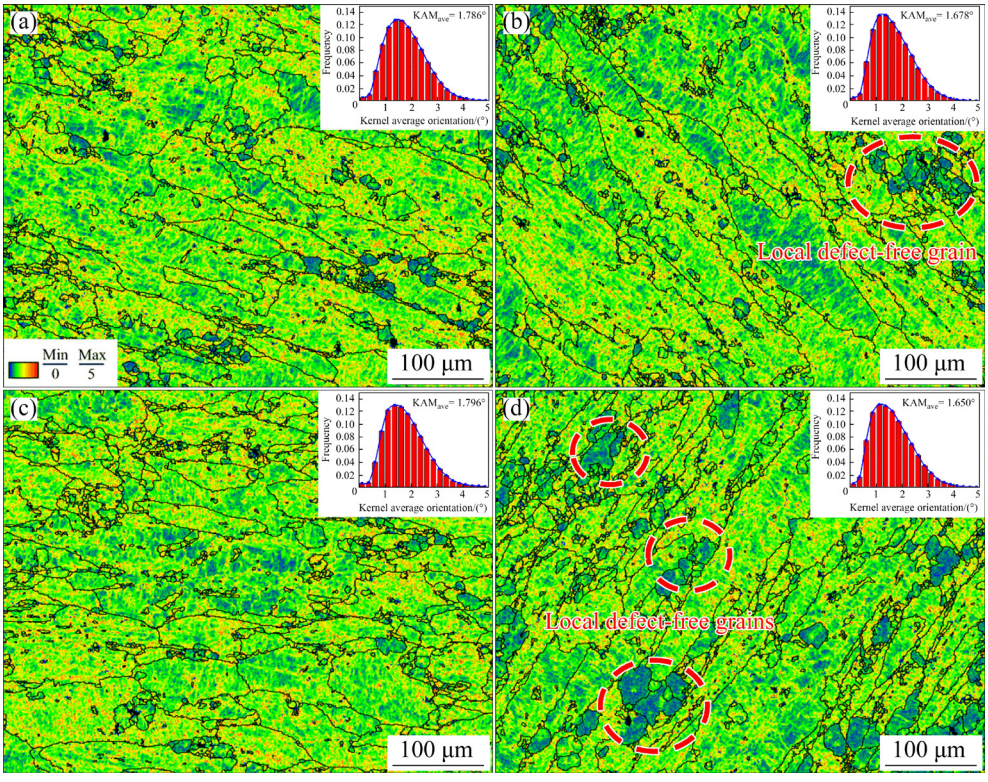

Fig. 10 KAM maps of Points P_1 (a), I_1 (b), P_2 (c), and I_2 (d)

induced current, several small grains with low KAM values were generated in Points I_1 and I_2 due to dislocation movement within the grains to grain boundaries, leading to the formation of defect-free grains. Thus, the induced current removed high intra-grain dislocations, thereby recovering the material plasticity.

The electron wind formed by the collision of high-speed electrons with the nuclei under the action of current would favor the mobility of dislocations [23], while the electron wind force is proportional to the current density. According to induced current density simulations (Section 4.1), the induced current with a peak value of 10^5 kA/mm^2 passed through the specimen during the IEPT. Thus, the pulse current accelerated the movement of dislocations, as well as resulted in the dislocation annihilation and dislocation rearrangement within the material. TANG et al [24] noticed an increase in the combination of dipole dislocations under electron wind-driven effect with promoted dislocation sliding towards grain boundaries to accelerate dislocation annihilation and reduce dislocation density.

Induced currents may promote dislocation motion and annihilation, thereby altering dislocation density and dislocation entanglement. The changes in the internal dislocation arrangement of the grains before and after IEPT are shown in Fig. 11. The internal dislocations of pre-deformed grains looked highly entangled (Fig. 11(a)). As for the specimen after IEPT, the internal dislocation density was significantly reduced, and dislocation entanglement caused by pre-deformation became dispersed. XIANG et al [25] studied the effects of high current-density electrical pulses (10^3 A/mm^2) on residual stresses in quenched steel. Their data revealed that enhancement in motion of vacancies and dislocations in the presence of drifting electrons did not only accelerate the annihilation of dislocations but also formed dislocations oriented within the crystal in the direction of electron drift. The details of dislocation morphology in Fig. 11(b) are shown in Fig. 11(c). After IEPT, the dislocations became parallel in a specific direction, and the mobility of dislocations was increased by the electromigration effect of the current, while dislocation rearrangement took place.

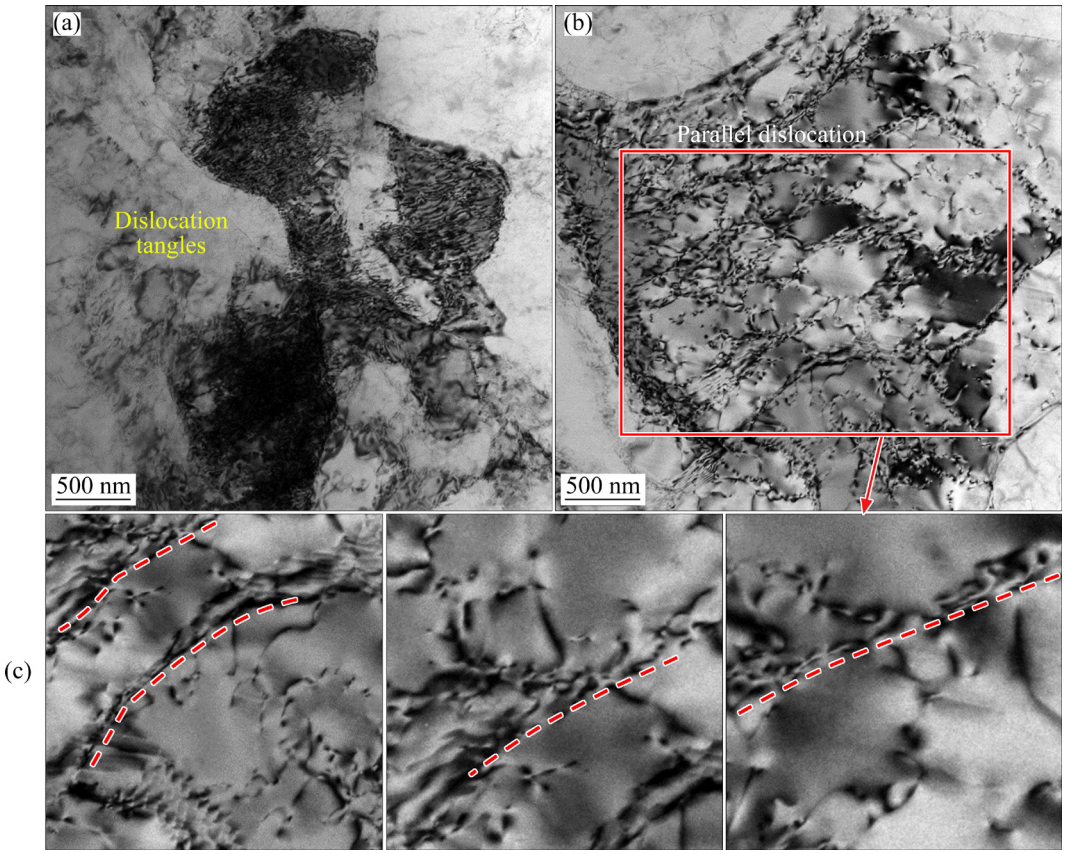

Fig. 11 TEM images of pre-deformed sample (a), IEPT-treated sample (b), and local enlargement of dislocation distribution (c) in (b)

4.3 Quantitative analysis of strength change

According to stress−strain curves, IEPT relieved material work hardening caused by pre-deformation. All specimens revealed a “stress drop” and increased elongation. Previous studies have shown that annealing Al−Mg alloys with pulsed currents during deformation results in lower flow stress [26]. Four known strengthening mechanisms have been reported: (1) strain hardening, (2) solid solution strengthening, (3) precipitation strengthening, and (4) fine-grain strengthening [27]. The experimental results displayed that the reduction in strength caused by IEPT was mainly attributed to changes in dislocation density and grain size. The first “stress drop” at 7% pre-deformation was selected for further analysis, and the strength change relationship can be expressed by Eq. (1):

$$\Delta\sigma=\Delta\sigma_{\mathrm{d}}+\Delta\sigma_{\mathrm{g}} \tag{1}$$

where $\Delta\sigma$ indicates the change in strength, $\Delta\sigma_{\mathrm{d}}$ refers to the variation in strength due to dislocation density change, and $\Delta\sigma_{\mathrm{g}}$ denotes the strength change due to grain size variation.

The dislocation density of the material was calculated using XRD, where the electron beam collides with targets to produce X-rays. The common target used for aluminum alloy calibration was often the Cu target. The wavelength of the Cu radiation used in Eq. (2) was kept constant to avoid affecting the results of the model equation. Figure 12 shows the XRD patterns of Points P_1 and I_1. The highest intensity peak was attributed to the (200) crystal plane. The peak intensity decreased significantly after IEPT, indicating induced current affecting the texture of the material. The XRD peak of (200) was used to calculate the peak broadening. The Williamson−Hall method was employed to calculate the grain diameter D and microstrain ε of bulk samples from the XRD peak broadening B using the following expression [28]:

$$B\cos\theta_{\mathrm{B}}=\frac{K\lambda}{D}+\varepsilon\sin\theta_{\mathrm{B}} \tag{2}$$

where λ is the wavelength of Cu K_α radiation (1.54056 Å), K is equal to 0.9, and θ_{B} is the Bragg angle.

The values of D and ε were obtained from the slope and intercept of the fitted curve after plotting $B\cos\theta_{\mathrm{B}}$ versus $\sin\theta_{\mathrm{B}}$ and performing a linear regression analysis [29]. The dislocation density ρ was calculated as follows [30]:

$$\rho=\frac{2\sqrt{3}\varepsilon}{Db} \tag{3}$$

where b(=0.286 nm) represents the magnitude of the Burgers vector for Al.

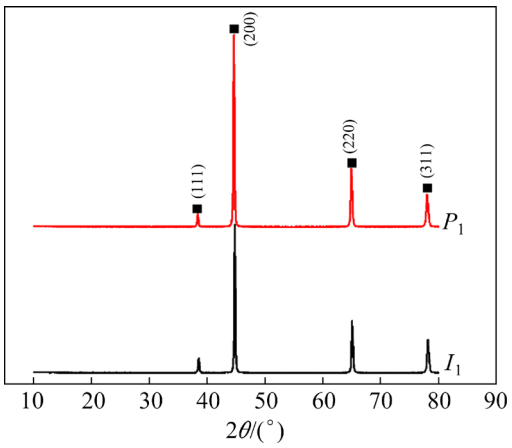

Fig. 12 XRD patterns of Points P_1 and I_1

The FWHM of the strongest peak (200) in the XRD spectrum was calculated with the help of Jade 6 software. The larger FWHM values correspond to higher dislocation densities. Based on D and ε values obtained from Eq. (2), the values of ρ for Points P_1 and I_1 were estimated to be 7.56×10^{14} and 4.04×10^{14} m^{-2}, respectively. The variation trend of dislocation density was consistent with the KAM value. The calculated dislocation densities were used to estimate the strength contribution. The contribution of dislocations to the change in strength ($\Delta\sigma_{\mathrm{d}}$) was calculated by Taylor’s law of hardening [31]:

$$\Delta\sigma_{\mathrm{d}}=\alpha MGb\left(\rho_2^{1/2}-\rho_1^{1/2}\right) \tag{4}$$

For FCC metals, α=0.2, M is the Taylor coefficient (3.1), G is the shear modulus (27 GPa), b=0.286 nm, and ρ_1 and ρ_2 are the dislocation densities of the samples after pre-deformation and IEPT treatments, respectively. By substituting the dislocation density in Eq. (3), the reduction in $\Delta\sigma_{\mathrm{d}}$ was found to be −35.48 MPa.

After IEPT, the grain size was enlarged to some extent owing to the energy released by dislocation annihilation and Joule heating. The effect of $\Delta\sigma_{\mathrm{g}}$ on strength can be calculated based on the Hall−Petch strengthening theory [32]:

$$\Delta\sigma_{\mathrm{g}}=k\left(d_2^{-1/2}-d_1^{-1/2}\right) \tag{5}$$

where d_1 and d_2 are the average grain sizes after pre-deformation and IEPT, respectively. The parameter k is a constant associated with the yield strength measurement and taken as 0.12 MPa/m$^{1/2}$. For Points P_1 and I_1, the average grain sizes were 4.61 and 4.99 μm, respectively. The grain size increased after IEPT, which contributed to the decrease in yield strength. The contribution of $\Delta\sigma_g$ was −2.18 MPa.

After IEPT, the strength calculated from the equations dropped from 227.4 to 189.7 MPa, while the tensile strength declined from 227.4 to 184 MPa (Fig. 3(c)). The theoretical calculations were close to the experimental data, proving the correctness of the mechanical model. ZHU et al [33] investigated the effect of high-density electric current on the delay of fatigue crack initiation. They proposed that the applied electric current had a delaying effect on crack initiation. This may have induced the deviation in strength calculation. As shown in Fig. 4, the grain size of Point I_1 did not change significantly after IEPT. Thus, dislocation density was the primary cause of strain-hardening relief, with grain size playing only a minor role. IPET weakened the work hardening of pre-deformed materials, causing dislocation densities to decrease while grain size to increase slightly. As a result, dislocation and grain-boundary strengthening was weakened, ultimately reducing the material strength.

5 Conclusions

(1) Compared to pre-deformed specimens, the yield strength of the materials was reduced and the plasticity was increased after IEPT. Smaller pre-deformation achieved the highest elongations. When multiple stretching of 5% and discharge were used, the elongation increased by 145% compared to the original 5052-H32 material.

(2) The effect of induced currents promoted grain boundary sliding and grain size growth, while the average KAM value within the grain decreased. The deformed grain content declined while the substructure content was enhanced after IEPT.

(3) The induced currents promoted dislocation migration, leading to dislocation annihilation and rearrangement, with parallel aligned dislocations observed within the grains. XRD analysis revealed a decline in the dislocation density of samples. The calculated strength after IEPT using theoretical equations agreed well with experimental data.

CRediT authorship contribution statement

Shi-peng WANG: Conceptualization, Methodology, Investigation, Writing − Original draft; **Xiao-hui CUI:** Validation, Writing − Review & Editing, Supervision, Funding acquisition; **Ang XIAO:** Investigation, Formal analysis, Writing − Review & Editing; **Zhuo-xing YU:** Conceptualization, Formal analysis, Visualization; **Zhi-hao DU:** Investigation, Formal analysis.

Declaration of competing interest

We declare that we do not have any commercial or associative interest that represents a conflict of interest in connection with the work.

Data availability statement

The raw data related to this manuscript will be made available upon request.

Acknowledgments

This work was supported by the National Natural Science Foundation of China (Nos. 51775563, 52275394), and the Project of State Key Laboratory of High-Performance Complex Manufacturing, Central South University, China (No. ZZYJKT2020-02).

References

[1] ZHAO Kun-min, FAN Rong, WANG Li-min. The effect of electric current and strain rate on serrated flow of sheet aluminum alloy 5754 [J]. Journal of Materials Engineering and Performance, 2016, 25(3): 781−789.

[2] WANG Jin-lian, XU Jun, PAN Feng. Effect of annealing on microstructure and properties of Er modified 5052 alloy [J]. Results in Physics, 2018, 10: 476−480.

[3] LIANG C L, LIN K L. The microstructure and property variations of metals induced by electric current treatment: A review [J]. Materials Characterization, 2018, 145: 545−555.

[4] NGUYEN T H, OH H, HONG S, HAN H N, CAO Jian, AHN S H, CHUN D M. A review of electrically-assisted manufacturing [J]. International Journal of Precision Engineering and Manufacturing−Green Technology, 2015, 2(4): 365−376.

[5] TIWARI J, PRATHEESH P, BEMBALGE O B, KRISHNASWAMY H, AMIRTHALINGAM M, PANIGRAHI S K. Microstructure dependent electroplastic effect in AA 6063 alloy and its nanocomposites [J]. Journal of Materials Research and Technology, 2021, 12: 2185−2204.

[6] DIMITROV N K, LIU Yu-cheng, HORSTEMEYER M F. Electroplasticity: A review of mechanisms in electro-mechanical coupling of ductile metals [J]. Mechanics of

Advanced Materials and Structures, 2022, 29(5): 705−716.

[7] ZHANG Xin, LI Hong-wei, ZHAN Mei, ZHENG Ze-bang, GAO Jia, SHAO Guang-da. Electron force-induced dislocations annihilation and regeneration of a superalloy through electrical in-situ transmission electron microscopy observations [J]. Journal of Materials Science & Technology, 2020, 36: 79−83.

[8] YAN Jia-wei, LI Wei, LIU Hai-ting, SHEN Yao. Reversion of sub-boundaries into dense dislocations in aluminum by electric pulsing treatment [J]. Scripta Materialia, 2019, 167: 86−90.

[9] LIU Kai, DONG Xiang-huai, SHI Wen. Effect of pulsed current on AZ31B magnesium sheets during annealing [J]. Transactions of Nonferrous Metals Society of China, 2019, 29(4): 735−740.

[10] ZHOU Chang, ZHAN Li-hua, LI He, ZHAO Xing, CHEN Fei, HUANG Ming-hui. Creep ageing behaviour assisted by electropulsing under different stresses for Al−Cu−Li alloy [J]. Transactions of Nonferrous Metals Society of China, 2021, 31(7): 1916−1929.

[11] ROH J, SEO J, HONG S, KIM M, HAN H N, ROTH J T. The mechanical behavior of 5052-H32 aluminum alloys under a pulsed electric current [J]. International Journal of Plasticity, 2014, 58: 84−99.

[12] CHEN Zhe, LI Bing, HUANG Qing-yu, ZHANG Lin, FEI Han-lin, LIU Jian. The effect of the electric pulse treatment on the microstructure and mechanical performance of the Al−Zn alloy [J]. Materials Science and Engineering A, 2020, 796: 140016.

[13] YANG C L, YANG H J, ZHANG Z J, ZHANG Z F. Recovery of tensile properties of twinning-induced plasticity steel via electropulsing induced void healing [J]. Scripta Materialia, 2018, 147: 88−92.

[14] GU Shao-jie, CUI Yi, KIMURA Y, TOKU Y, JU Yang. Relief of strain hardening in deformed Inconel 718 by high-density pulsed electric current [J]. Journal of Materials Science, 2021, 56(29): 16686−16696.

[15] DOBRAS D, BRUSCHI S, SIMONETTO E, RUTKOWSKA-GORCZYCA M, GHIOTTI A. The effect of direct electric current on the plastic behavior of AA7075 aluminum alloy in different states of hardening [J]. Materials, 2021, 14(1): 73.

[16] XIAO Ang, HUANG Chang-qing, CUI Xiao-hui, YAN Zi-qin, YU Zhuo-xing. Impact of the pulse induced current on the microstructure and mechanical properties of the 7075-T6 aluminum alloy [J]. Journal of Alloys and Compounds, 2022, 911: 165021.

[17] JIANG Yan-bin, TANG Guo-yi, SHEK C, LIU Wei. Microstructure and texture evolution of the cold-rolled AZ91 magnesium alloy strip under electropulsing treatment [J]. Journal of Alloys and Compounds, 2011, 509: 4308−4313.

[18] SHENG Yin-ying, HUA You-lu, WANG Xiao-jian, ZHAO Xue-yang, CHEN Lian-xi, ZHOU Han-yu, WANG J, BERNDT C, LI Wei. Application of high-density electropulsing to improve the performance of metallic materials: Mechanisms, microstructure and properties [J]. Materials, 2018, 11(2): 185.

[19] PAN Dong, WANG Yi-tong, GUO Qing-tao, ZHANG Dong, XU Xiao-feng, ZHAO Yu-guang. Grain refinement of Al−Mg−Si alloy without any mechanical deformation and matrix phase transformation via cyclic electro-pulsing treatment [J]. Materials Science and Engineering A, 2021, 807: 140916.

[20] PANDEY A, KHAN A S, KIM E Y, CHOI S H, GNÄUPEL-HEROLD T. Experimental and numerical investigations of yield surface, texture, and deformation mechanisms in AA5754 over low to high temperatures and strain rates [J]. International Journal of Plasticity, 2013, 41: 165−188.

[21] FAN R, MAGARGEE J, HU Ping, CAO Jian. Influence of grain size and grain boundaries on the thermal and mechanical behavior of 70/30 brass under electrically-assisted deformation [J]. Materials Science and Engineering A, 2013, 574: 218−225.

[22] BREWER L N, OTHON M A, YOUNG L M, ANGELIU T M. Misorientation mapping for visualization of plastic deformation via electron back-scattered diffraction [J]. Microscopy and Microanalysis, 2006, 12(1): 85−91.

[23] KRISHNASWAMY H, KIM M J, HONG S T, KIM D, SONG J H, LEE M G, HAN H N. Electroplastic behaviour in an aluminium alloy and dislocation density based modelling [J]. Materials & Design, 2017, 124: 131−142.

[24] TANG Yong-peng, ATSUSHI H, YUICHI I, JU Yang. Effect of high-density electric current on the microstructure and fatigue crack initiation of stainless steel [J]. Materials Transactions, 2013, 54(11): 2085−2092.

[25] XIANG Si-qi, ZHANG Xin-fang. Dislocation structure evolution under electroplastic effect [J]. Materials Science and Engineering A, 2019, 761: 138026.

[26] KIM M J, LEE K, OH K H, CHOI I S, YU H H, HONG S T, HAN H N. Electric current-induced annealing during uniaxial tension of aluminum alloy [J]. Scripta Materialia, 2014, 75: 58−61.

[27] QIN Wen-bo, LI Jian-sheng, LIU Yao-yao, KANG Jia-jie, ZHU Li-na, SHU Deng-feng, PENG Peng, SHE Ding-shun, MENG D, LI Yu-sheng. Effects of grain size on tensile property and fracture morphology of 316L stainless steel [J]. Materials Letters, 2019, 254: 116−119.

[28] XU Ping-wei, LUO Hong-yun, HAN Zhi-yuan, ZOU Jian. Tailoring a gradient nanostructured age-hardened aluminum alloy using high-gradient strain and strain rate [J]. Materials & Design, 2015, 85: 240−247.

[29] MA Ka-ka, WEN Hai-ming, HU Tao, TOPPING T D, ISHEIM D, SEIDMAN D N, LAVERNIA E J, SCHOENUNG J M. Mechanical behavior and strengthening mechanisms in ultrafine grain precipitation-strengthened aluminum alloy [J]. Acta Materialia, 2014, 62: 141−155.

[30] WEN Hai-ming, TOPPING T D, ISHEIM D, SEIDMAN D N, LAVERNIA E J. Strengthening mechanisms in a high-strength bulk nanostructured Cu–Zn–Al alloy processed via cryomilling and spark plasma sintering [J]. Acta Materialia, 2013, 61: 2769−2782.

[31] DAVOUDI K M, VLASSAK J J. Dislocation evolution during plastic deformation: Equations vs. discrete dislocation dynamics study [J]. Journal of Applied Physics, 2018, 123(8): 85302.

[32] LOUCIF A, FIGUEIREDO R B, BAUDIN T, BRISSST F, CHEMAM R , LANGDON T G. Ultrafine grains and the Hall−Petch relationship in an Al−Mg−Si alloy processed by

high-pressure torsion [J]. Materials Science and Engineering A, 2012, 532: 139−145.
[33] ZHU Y H, TO S, LEE W B, LIU X M, JIANG Y B, TANG G Y. Effects of dynamic electropulsing on microstructure and elongation of a Zn−Al alloy [J]. Materials Science and Engineering A, 2009, 501: 125−132.

多道次拉伸和感应电流处理 5052 铝合金的力学性能和显微组织演变

王世鹏[1]，崔晓辉[1,2,3]，肖 昂[2]，余卓行[2]，杜志浩[2]

1. 中南大学 轻合金研究院，长沙 410083；
2. 中南大学 机电工程学院，长沙 410083；
3. 中南大学 高性能复杂制造国家重点实验室，长沙 410083

摘 要：提出一种多道次拉伸和感应电流处理(IEPT)相结合的复合成形方法，采用 TEM 和 EBSD 揭示感应电流对材料显微组织和力学性能的影响规律。结果表明，采用 4 次拉伸 5%和拉伸后放电，材料伸长率比原始材料增加 145%。预拉伸试样经过 IEPT 处理后，强度下降、塑性提高，材料的位错密度下降，晶粒变形结构向亚结构转变，同时晶粒尺寸略有增加。感应电流减弱材料的各向异性，出现新的⟨111⟩//TD 织构。电塑性效应和焦耳热效应的结合增强位错运动和空位移动。采用 ANSYS 软件模拟板料的温度分布，最高温度达到 144.7 ℃。材料强度的理论计算结果与实验数据一致。

关键词：5052 铝合金；感应电流；织构演变；焦耳热模拟；强度计算

(Edited by Bing YANG)